J. Fluid Mech. (2023), *vol*. 965, A11, doi:10.1017/jfm.2023.398

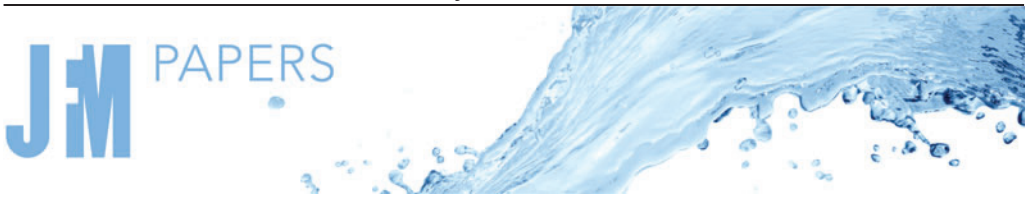

The axisymmetric screech tones of round twin jets examined via linear stability theory

Michael N. Stavropoulos[1],†, Matteo Mancinelli[2], Peter Jordan[3], Vincent Jaunet[3], Joel Weightman[1], Daniel M. Edgington-Mitchell[1] and Petrônio A.S. Nogueira[1]

[1]Department of Mechanical and Aerospace Engineering, Laboratory for Turbulence Research in Aerospace and Combustion, Monash University, Clayton 3800, Australia

[2]Department of Civil, Computer Science and Aeronautical Technologies Engineering, Università degli Studi Roma Tre, Via Vito Volterra 62, 00146 Rome, Italy

[3]Département Fluides, Thermique, Combustion, Institut Pprime, CNRS-Université de Poitiers-ENSMA, Poitiers, France

(Received 28 October 2022; revised 27 March 2023; accepted 2 May 2023)

Spatial linear stability analysis is used to study the axisymmetric screech tones generated by twin converging round nozzles at low supersonic Mach numbers. Vortex-sheet and finite-thickness models allow for identification of the different waves supported by the flow at different conditions. Regions of the frequency–wavenumber domain for which the upstream-propagating guided jet modes are observed to be neutrally stable are observed to vary as a function of solution symmetry, jet separation, S, and the velocity profile used. Screech-frequency predictions performed using wavenumbers obtained from both models agree well with experimental data. Predictions obtained from the finite-thickness model better align with the screech tones measured experimentally and so are seen to be an improvement on predictions made with the vortex sheet. Additionally, results from the finite-thickness model predict both symmetric and antisymmetric screech tones for low S that are found in the vortex-sheet model only at greater S. The present results indicate that the feedback loop generating these screech tones is similar to that observed for single-jet resonance, with equivalent upstream and downstream modes.

Key words: jet noise, shear-flow instability, jets

† Email address for correspondence: michael.stavropoulos@monash.edu

1. Introduction

Screech tones are observed in jets operating away from their design Mach number, appearing as high-amplitude discrete peaks in the acoustic spectrum. Along with broadband shock-associated noise (BBSAN) and turbulent-mixing noise, they form the three components of supersonic jet noise (Tam 1995). The appearance of screech tones is undesirable due to both the high intensity noise emitted and the potential to induce vibrations in the surrounding structure, which can lead to failure (Berndt 1984; Raman, Panickar & Chelliah 2012). These characteristics of screech tones have led to many studies on understanding and mitigating the phenomenon, as shown by reviews from Raman (1999) and Edgington-Mitchell (2019).

Jets from round convergent nozzles exhibit screech in discrete modal stages that can be classified into the A1 and A2 axisymmetric modes, the C helical mode and the B and D flapping modes (Merle 1957; Davies & Oldfield 1962; Powell, Umeda & Ishii 1992). Powell (1953*a*,*b*) first described screech as arising from a resonance feedback loop within the jet. This loop is comprised of four stages (Edgington-Mitchell 2019). The first is a downstream-propagating disturbance, which travels with the flow until reaching some point downstream. At this downstream point there is a conversion from a downstream-propagating disturbance into an upstream-propagating one. This upstream-propagating disturbance then travels back until reaching an upstream reflection point, where it creates a new downstream-propagating disturbance, completing the resonance loop. The present work here considers free jets and, thus, the upstream and downstream reflection points take the form of the nozzle plane and shock-cell structure, respectively.

A better understanding of screech can only be achieved through knowledge of the underlying physics involved in each step of the resonance cycle. Since the identification of coherent structures in high-speed jets, by Mollo-Christensen (1967) and Crow & Champagne (1971), was previously considered to be dominated by stochastic processes, considerable effort has been directed towards the modelling and prediction of these structures. For jet screech, such modelling involves considering the forms that the downstream- and upstream-propagating disturbances take. Initially these were modelled to take the form of a Kelvin–Helmholtz (KH) instability and a free-stream sound wave, respectively (Powell 1953*b*). Recent results have shown that the upstream-travelling mode is a guided jet mode, first studied by Tam & Hu (1989) and known to exist over a finite frequency range (Towne *et al.* 2017). The work of Shen & Tam (2002) was the first to consider the upstream-propagating guided jet mode (k_p^-) as the closure mechanism for the resonance loop in a free jet. They proposed that whilst screech modes A1 and B were still closed by the free-stream acoustic mode, it was the k_p^- mode that closed resonance for the A2 and C modes. The finite existence region, frequencies over which the mode is propagative for a given set of jet parameters, of the k_p^- mode was considered by both Gojon, Bogey & Mihaescu (2018) and Edgington-Mitchell *et al.* (2018) for a single jet. In these works the A1 and A2 screech modes were shown to be encompassed by the frequencies defining this existence region, and so could be explained by the characteristics of the k_p^- mode.

Screech-frequency predictions were then performed using a vortex-sheet model for a single jet by Mancinelli *et al.* (2019). This followed the resonance criteria set out in Landau & Lifshitz (2013), later applied to the case of jet-edge interactions by Jordan *et al.* (2018). These predictions were made considering a k_p^- mode and showed close agreement with experiments, in contrast with the poor agreement achieved by considering resonance to be closed by free-stream sound waves. Later, Mancinelli *et al.* (2021)

showed that improvements could be made in these screech-frequency predictions by instead considering a finite-thickness model. The presence of the k_p^- mode in the resonance cycle was also confirmed both experimentally and by linear stability analysis in Edgington-Mitchell *et al.* (2021). Following the hypothesis of Tam & Tanna (1982) they showed that the interaction between the KH mode and the shock-cell structure gives rise to new waves in the flow that may close the resonance loop. Recent work by Edgington-Mitchell *et al.* (2022) expanded on this and demonstrated that the modal staging behaviour of screech could be explained when considering interactions involving the sub-optimal wavenumbers describing the shock-cell structure. Such sub-optimal wavenumbers arise when taking a Fourier transform of the mean flow in the axial direction and represent the axial variations of the shock-cell structure (Nogueira *et al.* 2022*a*). Nogueira *et al.* (2022*b*) has verified the hypothesis of Tam & Tanna (1982), showing how screech is underpinned by an absolute instability mechanism involving the k_p^- mode and the KH mode, providing a characterisation of the phenomenon in line with early descriptions based on experiments such as Powell (1953*b*).

Additional complexities arise when considering a twin jet due to acoustic and hydrodynamic interactions between the two jets. This is highlighted in an early study by Seiner, Manning & Ponton (1988), where pressure amplitudes where found to be more than double the single jet equivalent. Screech tones in a twin-jet system use the same naming convention as for the single jet, with the exception that C is a flapping mode as the system has been shown not to support helical modes (Rodríguez *et al.* 2022). Previous studies (Bell *et al.* 2018; Knast *et al.* 2018) considered the coupling dynamics at play between the two jets. Bell *et al.* (2021) later showing that a round twin-jet system exhibits intermittent coupling and at some jet operating conditions can uncouple entirely. This behaviour was proposed to be due to competition between modes of the flow associated with the different symmetries. The twin-jet vortex sheet was considered previously first by Sedel'Nikov (1967*a*), Morris (1990) and later Du (1993). While in these works the characteristics of both the upstream- and downstream-propagating waves were considered, their roles in resonance were not explored directly. Interest in modelling was renewed by Rodríguez, Jotkar & Gennaro (2018) and Nogueira & Edgington-Mitchell (2021). The former studied KH instabilities in subsonic twin jets using parabolised stability equations, whilst the latter applied a spatial stability analysis to explore coupling and resonance behaviour of a supersonic twin-jet system with an ideally expanded jet Mach number (M_j) of 1.7. This latter study linked the k_p^- mode to twin-jet resonance at those specific conditions. The analysis was limited to a single set of jet conditions for which experimental data was available. The success of linear stability analysis in predicting the coherent structures and screech characteristics in this previous work suggests such a framework may shed light on the underlying resonance mechanism for other conditions.

In this work, linear stability analysis will be performed for the twin-jet system using both vortex-sheet and finite-thickness models, with comparisons made to experimental acoustic data. The parameter space will be limited to relatively low supersonic Mach numbers where the system exhibits axisymmetric screech modes, as prior modelling efforts for single screeching jets indicate that the vortex-sheet approximation performs best at these conditions (Mancinelli *et al.* 2019, 2021).

The paper is organised as follows. The twin-jet set-up and experimental methodology are detailed in § 2. In § 3 the mathematical models for both the vortex-sheet, finite-thickness and screech-frequency prediction models are outlined. Results are shown in § 4, with concluding remarks made in § 5.

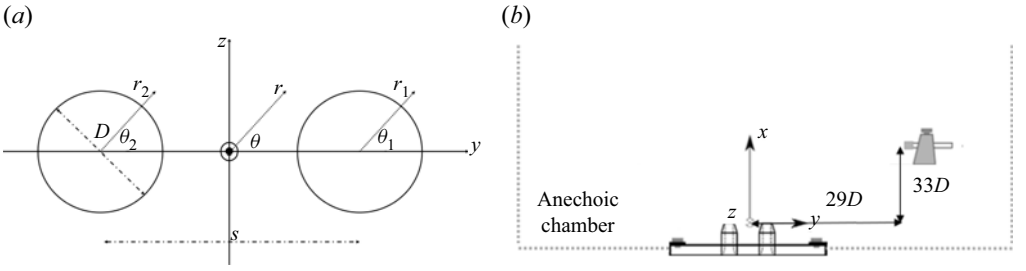

Figure 1. (*a*) Twin-jet set-up and (*b*) experimental set-up.

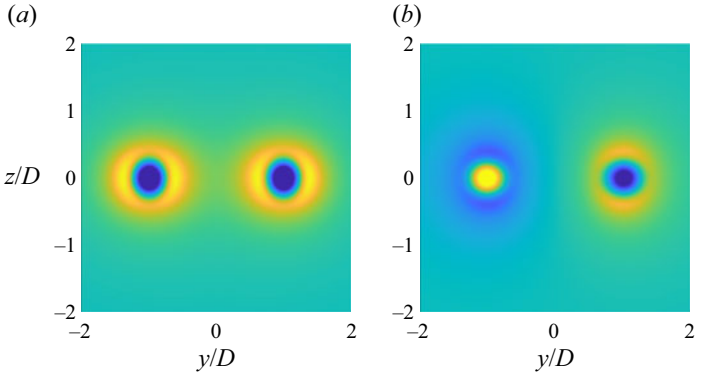

Figure 2. Visualisation of the twin-jet solution symmetries considered in this work, (*a*) SS and (*b*) SA. Shown are the real components of the k_p^- (0, 2) pressure eigenfunctions found using the finite-thickness twin-jet model with $S = 2$, $Mj = 1.16$, $St = 0.69$, $\delta = 0.2$.

2. Set-up

The round twin-jet set-up considered here is as shown in figure 1(*a*) with x the axial direction orientated out of the page. Each jet is of diameter D and has an individual coordinate system, (r_1, θ_1) and (r_2, θ_2), in r and θ. The separation of the jets is measured centre-to-centre and denoted by S, which is normalised by D. In this configuration solutions can be classified based on their symmetries about the x–y and x–z planes. These solutions are classified as SS, SA, AS and AA (Rodríguez *et al.* 2018), which is the convention now commonly used in the literature among both round (Nogueira & Edgington-Mitchell 2021; Stavropoulos *et al.* 2022) and rectangular (Yeung, Schmidt & Brès 2022) twin-jet studies. The first letter (S or A) denotes symmetry or antisymmetry about the x–y plane and the second about the x–z plane. These symmetries are visualised in figure 2. In the present work attention is focused solely on the axisymmetric, A1 and A2, screech modes. As such, only twin-jet symmetries that allow axisymmetric solutions will be investigated. This results in only the SS and SA symmetries being considered as AS and AA symmetries cannot support axisymmetric solutions.

Acoustic measurements were taken at the supersonic jet anechoic facility (SJAF) in the Laboratory for Turbulence Research in Aerospace and Combustion (LTRAC) at Monash University. Details on the facility can be found in Wong *et al.* (2020) with the nozzle plate design described in Knast *et al.* (2018). The twin-jet nozzles have an exit diameter of 8 mm and are purely converging unheated jets. Measurements are taken using a GRAS Type 46BE 1/4 in. pre-amplified free-field microphone with a frequency range

of 4 Hz–100 kHz, calibrated using a GRAS 42AB sound calibrator. It is positioned at a distance of 33D downstream and 29D in the radial direction, taken from the centre of the system as seen in figure 1(b). For each spacing, the nozzle pressure ratio (NPR) was varied from 2–2.5 in increments of 0.025, with a total of 1M samples obtained at an acquisition frequency of 200 kHz for each NPR. Acoustic power spectral densities (PSD) are obtained through a fast Fourier transform applied using the Welch method (Welch 1967) with 75 % overlap for 4096 points to ensure a fine discretisation in frequency.

3. Mathematical models

3.1. *Vortex-sheet model*

In the vortex-sheet approximation the jet boundary is represented by an infinitesimal shear layer (Lessen, Fox & Zien 1965; Sedel'Nikov 1967*b*; Michalke 1970; Morris 2010). Within the locally parallel framework, the streamwise velocity is taken as constant within the jet and zero outside of it. Following Morris (1990) and Du (1993) the flow is divided into mean and perturbed components. Applying the normal mode ansatz to the perturbed component, the pressure field may be written as

$$\tilde{P}(x, r_{1,2}, \theta_{1,2}, t) = P(r_{1,2}, \theta_{1,2})\, \mathrm{e}^{-\mathrm{i}\omega t + \mathrm{i}kx}, \tag{3.1}$$

with k the wavenumber and ω the angular frequency. Upon substitution into the Euler equations this allows an equation for the perturbed pressure amplitude to be written as

$$\frac{\partial^2 P}{\partial r_{1,2}^2} + \frac{1}{r_{1,2}}\frac{\partial P}{\partial r_{1,2}} + \frac{1}{r_{1,2}^2}\frac{\partial^2 P}{\partial \theta_{1,2}^2} - \lambda_{i,o}^2 P = 0, \tag{3.2}$$

where subscripts i and o denote inner, within the jet, and outer, outside of the jet, solutions, respectively, and

$$\left.\begin{aligned} \lambda_i &= \sqrt{k^2 - \frac{1}{T}(\omega - Mk)^2}, \\ \lambda_0 &= \sqrt{k^2 - \omega^2}. \end{aligned}\right\} \tag{3.3}$$

Here M is the acoustic Mach number and T the temperature ratio between jet and free stream. Quantities are normalised using the free-stream density, free-stream sound speed and jet diameter. Solutions of this equation for both inner and outer regions expressed in forms consistent with the symmetry classification defined above are given by

$$P_i(r_{1,2}, \theta_{1,2}) = \sum_{m=0}^{\infty} \hat{A}_m \mathrm{I}_m(\lambda_i r_{1,2}) \cos(m\theta_{1,2}) + \hat{B}_m \mathrm{I}_m(\lambda_i r_{1,2}) \sin(m\theta_{1,2}), \tag{3.4}$$

$$P_o(r_1,\theta_1,r_2,\theta_2) = \sum_{m=0}^{\infty} A_m[\mathrm{K}_m(\lambda_0 r_1)\cos(m\theta_1) + (-1)^m \mathrm{K}_m(\lambda_0 r_2)\cos(m\theta_2)] + \sum_{m=0}^{\infty} B_m[\mathrm{K}_m(\lambda_0 r_1)\cos(m\theta_1) - (-1)^m \mathrm{K}_m(\lambda_0 r_2)\cos(m\theta_2)] + \sum_{m=1}^{\infty} C_m[\mathrm{K}_m(\lambda_0 r_1)\sin(m\theta_1) - (-1)^m \mathrm{K}_m(\lambda_0 r_2)\sin(m\theta_2)] + \sum_{m=1}^{\infty} D_m[\mathrm{K}_m(\lambda_0 r_1)\sin(m\theta_1) + (-1)^m \mathrm{K}_m(\lambda_0 r_2)\sin(m\theta_2)], \quad (3.5)$$

with m the azimuthal mode number and I_m, K_m the modified Bessel functions of first and second kind, respectively. Each line of (3.5) corresponds to one of the four solutions, SS, SA, AS, AA mentioned previously. In (3.4) the first term corresponds to SS and SA symmetry, whilst the second to AS and AA symmetry.

To proceed further it is necessary to re-cast the outer solution into a function of only a single coordinate system. This is shown just for the SS symmetry solution and can be achieved through the Bessel addition formula (Lee & Chen 2011), such that

$$\mathrm{K}_m(\lambda_0 r_2)\cos(m\theta_2) = \sum_{n=-\infty}^{\infty} (-1)^n \mathrm{K}_{m-n}(\lambda_0 S)\mathrm{I}_n(\lambda_0 r_1)\cos(n\theta_1). \quad (3.6)$$

Equation (3.6) can then be substituted into (3.5) which, after simplification, yields

$$P_o(r_1,\theta_1) = \sum_{n=0}^{\infty} A_n \delta_{mn} \mathrm{K}_n(\lambda_0 r_1)\cos(n\theta_1) + (-1)^n \epsilon_n \mathrm{I}_n(\lambda_0 r_1)\cos(n\theta_1) \sum_{m=0}^{\infty} A_m (-1)^m [\mathrm{K}_{m-n}(\lambda_0 S) + \mathrm{K}_{m+n}(\lambda_0 S)], \quad (3.7)$$

with δ_{mn} the Kronecker delta and $\epsilon_n = 0.5$ for $n = 0$, and $\epsilon_n = 1$ otherwise. Inner and outer solutions are matched at the ideally expanded jet diameter, D_j, itself normalised by jet diameter and calculated following Tam & Tanna (1982) with a design Mach number of 1. Boundary conditions applied are continuity of pressure and displacement (Morris 2010). These are given by

$$P_i\left(\frac{D_j\lambda_i}{2}\right) = P_o\left(\frac{D_j\lambda_o}{2}\right), \quad (3.8)$$

$$\frac{\partial P_i}{\partial r_{1,2}}_{|r_{1,2}=0.5D_j} = \frac{1}{T}\frac{(\omega - kM)^2}{\omega^2}\frac{\partial P_0}{\partial r_{1,2}}_{|r_{1,2}=0.5D_j}. \quad (3.9)$$

Equations (3.4), (3.7), (3.8) and (3.9) can now be combined into a single dispersion relation for the twin-jet system as

$$\sum_{m=0}^{\infty} A_m[a_{nn}\delta_{mn} \pm (-1)^m c_{mn}] = 0, \quad (3.10)$$

Symmetry	(3.12)	(3.10)
SS	+	+
SA	+	−
AS	−	−
AA	−	+

Table 1. Value of ± terms in twin-jet vortex-sheet model for each solution symmetry.

with

$$a_{nn} = \frac{1}{\left(1 - \dfrac{kM}{\omega}\right)^2} - \frac{1}{T}\frac{\lambda_o}{\lambda_i}\frac{\mathrm{K}_n'\left(\dfrac{D_j\lambda_0}{2}\right)\mathrm{I}_n\left(\dfrac{D_j\lambda_i}{2}\right)}{\mathrm{I}_n'\left(\dfrac{D_j\lambda_i}{2}\right)\mathrm{K}_n\left(\dfrac{D_j\lambda_0}{2}\right)}, \tag{3.11}$$

$$c_{mn} = (-1)^n\epsilon_n[\mathrm{K}_{m-n}(\lambda_0 S) \pm \mathrm{K}_{m+n}(\lambda_0 S)]\left[\frac{\mathrm{I}_n\left(\dfrac{D_j\lambda_0}{2}\right)}{\mathrm{K}_n\left(\dfrac{D_j\lambda_0}{2}\right)}\frac{1}{\left(1 - \dfrac{kM}{\omega}\right)^2} - \frac{1}{T}\frac{\lambda_o}{\lambda_i}\frac{\mathrm{I}_n\left(\dfrac{D_j\lambda_i}{2}\right)\mathrm{I}_n'\left(\dfrac{D_j\lambda_0}{2}\right)}{\mathrm{K}_n\left(\dfrac{D_j\lambda_o}{2}\right)\mathrm{I}_n'\left(\dfrac{D_j\lambda_i}{2}\right)}\right]. \tag{3.12}$$

The ± in (3.10) and (3.12) are used to define symmetry or antisymmetry about both the x–z and x–y planes as detailed in table 1. A key difference between the dispersion relation for the twin jet and the single jet, studied by Lessen *et al.* (1965), Michalke (1970) and Towne *et al.* (2017), is that the former is unable to be solved for only a single azimuthal mode number, m. Instead, by truncating (3.10) to a finite value (N) the system is solved for all m up to $N - 1$ for both SS and SA modes.

Equation (3.10) is solved with $N = 20$ for all calculations, with convergence checked up to $N = 50$. It is worth noting that (3.11) takes the exact same form as the dispersion relation for a single jet as shown by Towne *et al.* (2017). This allows for recovery of the single-jet solution at large S, as (3.12) tends to 0 as $S \to \infty$. On this basis, classification of twin-jet solutions is defined based on the equivalent single-jet solution they tend to at large spacing. For a given ω, any value of k that satisfies (3.10) is an eigenvalue of the vortex sheet, and (3.4) and (3.5) are used to build the corresponding pressure eigenfunctions.

3.2. *Finite-thickness model*

The finite-thickness formulation used here was developed initially by Lajús *et al.* (2019) and later applied to twin-jet systems by Nogueira & Edgington-Mitchell (2021). All parameters are non-dimensionalised by the free-stream sound speed and density, and jet diameter. The compressible Euler equations in polar coordinates are linearised assuming disturbances of the form

$$\tilde{P}(x, r, \theta, t) = P(r, \theta)\,\mathrm{e}^{\mathrm{i}(kx - \omega t)}, \tag{3.13}$$

with k and ω the non-dimensional streamwise wavenumber and frequency, respectively, and $\tilde{P}$ representing the pressure perturbations. With the linearised Euler equations written

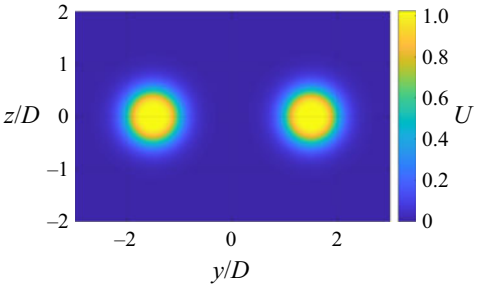

Figure 3. Sample twin-jet mean flow, U, used for the finite-thickness model for $M_j = 1.16$, $S = 3$, $\delta = 0.2$.

in polar coordinates, the symmetry of the mean flow imposes a θ periodicity in the coefficients of the equations, as $\bar{P}(r, \theta) = \bar{P}(r, \theta + n\pi)$ with n an integer. Using this periodicity, disturbances may be written with the Floquet ansatz

$$P(r, \theta) = \hat{P}(r, \theta)\mathrm{e}^{\mathrm{i}\mu\theta}, \tag{3.14}$$

where μ is the Floquet exponent, associated with the different symmetries supported by the flow. Computations then need only be done on a subsection of the azimuthal domain (for this case, in the interval $\theta = [-\pi/2, \pi/2)$ from figure 1*a*), reducing the computational cost; disturbances are extended to the entire cross-plane via (3.14). This leads to a generalised eigenvalue problem, expressed here in terms of pressure, of the form

$$\boldsymbol{L}\hat{P} = k\boldsymbol{R}\hat{P}, \tag{3.15}$$

with operators $\boldsymbol{L}$ and $\boldsymbol{R}$ functions of the mean flow, its derivatives and flow variables ω, M_j, S, μ and the ratio of specific heats γ. When solving, a Fourier discretisation is used in azimuth and Chebyshev polynomials in radius (Trefethen 2000), with boundary conditions imposed following Nogueira & Edgington-Mitchell (2021), and the matrix operators described in Appendix A. The numerical mapping of Bayliss & Turkel (1992) is applied to ensure appropriate resolution in the shear layer of the jets. Sparsity of the system is also considered, which further reduces the computational cost of the method.

This formulation introduces the need for a velocity profile as an input, which is not required when using the vortex-sheet model. Two hyperbolic tangent velocity profiles, one for each jet, of the same form used in Michalke (1971),

$$U(r) = M\left[0.5 + 0.5\tanh\left(\left(\frac{R_j}{r} - \frac{r}{R_j}\right)\frac{1}{2\delta}\right)\right], \tag{3.16}$$

are considered following Nogueira *et al.* (2022*a*) with M the acoustic Mach number, R_j the ideally expanded jet radius and δ used to characterise the shear-layer thickness. The corresponding twin-jet mean flow is then constructed through the addition of these two single-jet mean flows, following Rodríguez (2021). In each case, the mean temperature is obtained from (3.16) through the Crocco–Busemann relation. An example of a typical mean flow used is provided in figure 3, here visualised over both jets. Equation (3.15) is solved over a domain length of $4S$; a domain length of $8S$ was found to yield negligible change in the computed wavenumbers.

3.3. *Prediction model*

Screech-frequency predictions are performed using the model developed in Jordan *et al.* (2018) and Mancinelli *et al.* (2019, 2021), applied in these previous works to jet-edge interaction tones and for single-jet screech, respectively. This model considers two reflection points in the flow: the first (upstream) is the nozzle lip, where the KH mode is excited; the second (downstream) is the sth shock cell, where the upstream wave is considered to be generated (Mancinelli *et al.* 2023). It may be used to impose both phase and amplitude criteria (Jordan *et al.* 2018; Mancinelli *et al.* 2019, 2021). Following the neutral-mode assumption (Mancinelli *et al.* 2021), only the phase criterion is considered here,

$$k^+ - k_p^- = \frac{(2p+\phi)\pi}{L_s}, \tag{3.17}$$

with k^+ the real component of the KH mode wavenumber, p the number of cycles included in the resonance loop, ϕ the phase between reflection coefficients as a fraction of π and L_s the distance between the nozzle lip and the sth shock cell. This distance is given by

$$\left.\begin{aligned} L_1 &= \frac{\pi}{2.4048}\sqrt{M_j^2-1}, \\ L_s &= ((1-\alpha)s+\alpha)L_1, \end{aligned}\right\} \tag{3.18}$$

with $\alpha = 0.06$ the shock-cell length decrease rate with downstream distance (Harper-Bourne & Fisher 1974) and L_1 the first shock-cell length from Pack (1950). More recent considerations of (3.18) have also shown the strong alignment with it when compared with experiments (Mancinelli *et al.* 2021). The distances to each shock cell could also be computed via simulation, such as a Reynolds-averaged Navier–Stokes simulation (RANS); however, for the purpose of this work in drawing comparisons between the feedback loops in single and twin jets, the simple model of (3.18) is sufficient. For any pair of wavenumbers (k^+, k_p^-), obtained by solving (3.10) or (3.15), that satisfy (3.17) for given s, p and ϕ, the corresponding frequency is then a prediction of the screech frequency. As shown in Mancinelli *et al.* (2021), this resonance model can lead to similar frequency predictions compared with the absolute instability framework for the right choice of parameters. Note, however, that the specific values of p and s used for a given prediction are less important than the ratio of the two, p/s. For the specific case of $\phi = 0$, this ratio is equivalent to the ratio between the standing-wave wavenumber (k_{sw}) and the shock-cell wavenumber (k_s) (Mancinelli *et al.* 2021). As mentioned previously, multiple wavenumbers, dominant (k_{s1}) and sub-optimal (k_{s2}), are required to accurately describe the shock-cell variation (Nogueira *et al.* 2022*a*). Equation (3.17) does not consider sub-optimal wavenumbers and, thus, agreement between it and the wave interaction model outlined by Tam & Tanna (1982) occurs only when considering k_{s1}. Such agreement occurs for a value of $p/s = 1$ (Mancinelli *et al.* 2021). This indicates that any prediction using (3.17) with $p/s = 1$ corresponds to a consideration of the dominant wavenumber and anywhere $p/s \neq 1$ corresponds to the wavenumbers describing the axial variation in the shock-cell spacing.

4. Results

4.1. *Comparison to past formulations*

To validate the numerical implementation of (3.10), a comparison is performed with Morris (1990) and Du (1993) who had both previously calculated dispersion relation

Morris	*Du*	*Present study*
Type I	Family 1	SS
Type II	Family 4	AS
Type III	Family 2	SA
Type IV	Family 3	AA

Table 2. Symmetry notation for solutions of a twin-jet vortex sheet.

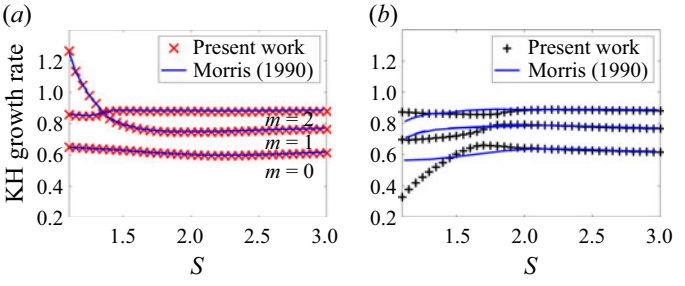

Figure 4. Comparison between the computed KH growth rates with those of Morris (1990) for (*a*) SS and (*b*) SA with $M_j = 1.32$ and $St = 1/\pi$. Note that growth rate values plotted here are scaled by jet radius.

eigenvalues of the twin-jet vortex-sheet model. These calculations were made for $M_j = 1.32$, $St = 1/\pi$ and a jet temperature ratio based on an isentropic expansion, where St is the non-dimensional frequency defined by $St = fD/U_j$. Only the symmetries SS and SA are considered for $m = 0, 1, 2$. The nomenclature for solution symmetry used in these previous works differs from the current convention with a guide between them provided in table 2, note that Du (1993) had mislabelled family 3 and 4 solutions that has been rectified in the present table. Figure 4(*a*) shows the results of Morris (1990) with those from (3.10) overlaid for SS symmetry. Plotted are the growth rates of the KH mode for the first three azimuthal modes. It can be seen that the results obtained here match the previous work. Conversely, in figure 4(*b*) the growth rates for SA do not match. A comparison between the current work and Du (1993) for both SS and SA growth rates is shown in figure 5, they can be seen to be in agreement; Du (1993) also noted a mismatch with the results of Morris (1990). Note that the formulation used here and in Du (1993) is identical to that provided in Morris (1990), suggesting that the discrepancy may arise due to an implementation error in the earlier work rather than a theoretical one. With the current twin-jet vortex-sheet model validated, it can be used with confidence for the remainder of this study. Details about the finite-thickness formulation can be found in Nogueira & Edgington-Mitchell (2021).

4.2. *Waves involved in screech*

4.2.1. *Characteristics of KH and k_p^- modes*

Before considering resonance, an overview of the behaviour of both the KH and k_p^- modes in a twin-jet system is considered. Eigenvalues of the dispersion relation calculated using (3.10) are plotted in figure 6, as in Tam & Hu (1989). Here results are presented for an isentropic temperature ratio, $M_j = 1.16$ and $S = 2$ and 50. In figure 6(*a*) classification in the form (m, n_r) of the relevant modes is highlighted, where m is the azimuthal mode number and n_r the radial mode number. The latter corresponds to the number of anti-nodes

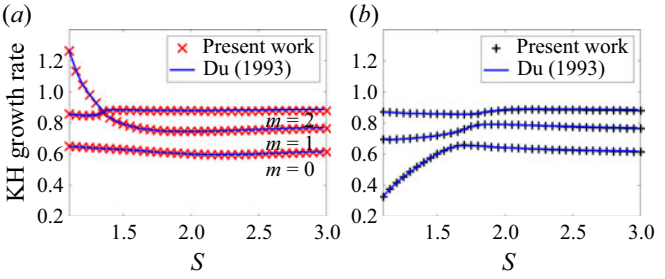

Figure 5. Comparison between the computed KH growth rates with those of Du (1993) for (*a*) SS and (*b*) SA with $M_j = 1.32$ and $St = 1/\pi$. Note that growth rate values plotted here are scaled by jet radius.

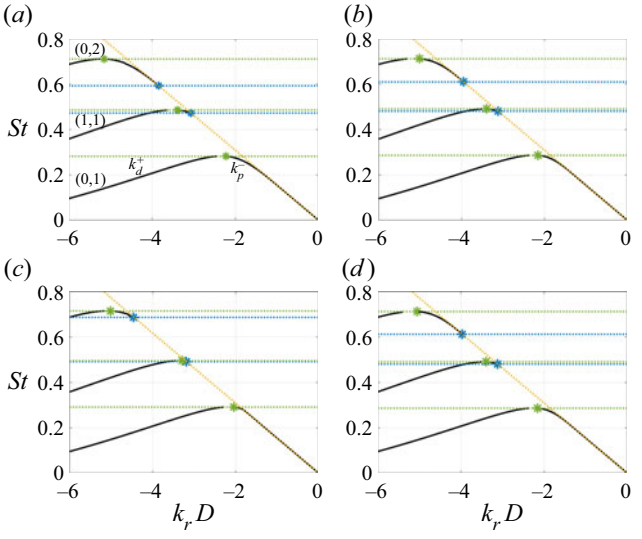

Figure 6. Dispersion relation eigenvalues for $M_j = 1.16$ for (*a*) SS, $S = 2$; (*b*) SS, $S = 50$; (*c*) SA, $S = 2$; and (*d*) SA, $S = 50$, plotted here are just modes corresponding to $m = 0$ and 1. Branch (blue) and saddle (green) points are highlighted. Also shown is the sonic line (yellow) for sound waves travelling upstream. Note that the green and blue bounds for the (1, 1) mode appear to be almost superimposed due to the close proximity of the branch and saddle points.

present in the pressure eigenfunction, as shown by (Tam & Hu 1989; Towne *et al.* 2017; Edgington-Mitchell *et al.* 2018; Gojon *et al.* 2018). Since the modes plotted here are neutrally convectively stable with negative phase speed, the sign of the slope indicates their propagation direction (group velocity): downstream-propagating waves, denoted k_d^+, have a positive slope, and k_p^- have a negative slope. Similar to the single-jet case (Tam & Hu 1989), it is observed that the k_p^- modes exist over a finite range of frequencies. The smallest frequency at which it exists is known as the branch point, and the highest frequency is characterised by a saddle point between k_d^+ and k_p^- (Towne *et al.* 2017). Comparing the results between figures 6(*a*) and 6(*c*), $S = 2$, with figures 6(*b*) and 6(*d*), $S = 50$, the existence region of the k_p^- $(0, 2)$ mode is strongly affected by the jet spacing only for SA. The branch points for SA are seen to decrease in value significantly as S increases, resulting in an increase in the k_p^- $(0, 2)$ existence region for increasing S. This trend suggests that coupling between the two jets may act to hinder the propagation of the SA

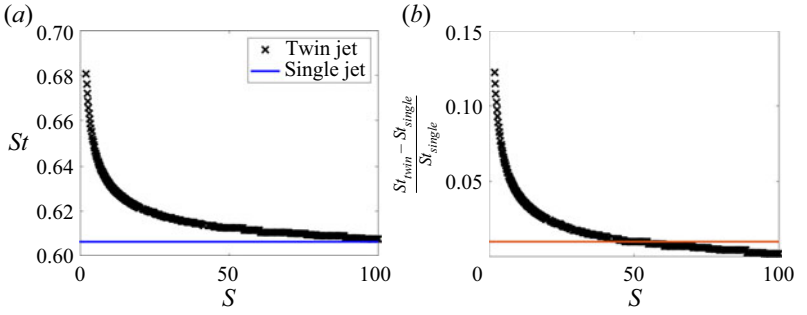

Figure 7. Comparison of SA k_p^- (0, 2) branch point with the single-jet value for the $M_j = 1.16$ jet. This is compared directly in (*a*) and as a fraction in (*b*), also marked on (*b*) in red is the line corresponding to a 1 % divergence from the single-jet value.

symmetry k_p^- mode. The changes observed for SS symmetry are significantly smaller, with a slight increase in the (1, 1) branch point and a slight (<1 %) decrease in the (0, 2) branch point. The existence region of the SA symmetry k_p^- is smaller than that of SS symmetry throughout figure 6. The dispersion relation plots for SS and SA display non-negligible differences between the two symmetries even at $S = 15$; this suggests that resonant modes may be coupled for high inter-jet distances, which has also been observed experimentally (Shaw 1990; Knast *et al.* 2018). The value of S chosen for figures 6(*b*) and 6(*d*) is such that it represents a jet separation where the twin-jet system can be considered to behave as a single-jet system. There does not currently exist a unique metric for determining at which S this occurs. For this work, we focus on the axisymmetric screech modes, for which the k_p^- (0, 2) mode and its frequency band of existence is of importance. As such, the metric considered will be the frequency discrepancy, in St, between the SA k_p^- (0, 2) branch point and that of the single jet. Figure 7(*a*) shows the change in SA branch point at $M_j = 1.16$ across S, where it can be seen to exhibit an asymptotic convergence towards the single-jet value. Highlighting that whilst it is at low S where the effect of the second jet is most relevant, there is still a non-negligible effect from the second jet even at greater S. Note that at higher S the difference in St becomes lower than the resolution used ($\Delta St = 0.0005$) resulting in the curve no longer appearing smooth. The fractional difference between the single- and twin-jet values is given across S in figure 7(*b*). Given the asymptotic behaviour, the condition for the twin-jet system behaving as single jets is defined as when this difference is equal to 0.01 (1 % difference between twin-jet and single-jet values). From figure 7(*b*) this would correspond to an S of 50. Hence, the use of $S = 50$ in figure 6 for comparison with the low spacing ($S = 2$) case. It is, however, important to recognise that the value of $S = 50$ holds only for considerations of the k_p^- (0, 2) branch point, for example, if instead the wavenumber or growth rates of the KH mode were considered then this would result in a much smaller value of S as these values converge more quickly to the single-jet value (Morris 1990; Rodríguez *et al.* 2022).

The amplitude structure of the k_p^- (0, 2) and KH mode eigenfunctions can be obtained from the vortex-sheet model using (3.4) and (3.5). This allows for differences in structure between SS and SA type solutions to be visualised. In figure 8(*a*) the eigenfunction structure for the KH mode are compared for SS and SA plotted along the y axis of figure 1. A key difference occurs in the region between the two jets: due to the symmetry of the problem, the SA solution is forced to reach zero pressure at the centre point, whereas the SS solution is forced to reach a zero pressure gradient. Outside of this region the two

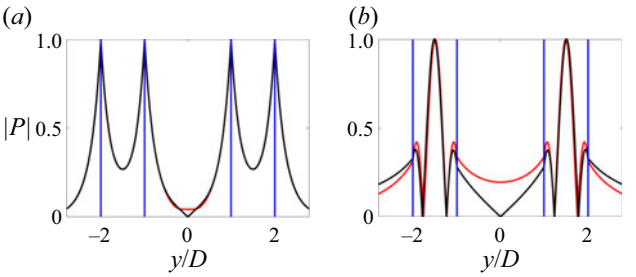

Figure 8. Absolute value of normalised pressure eigenfunctions along the y axis for SS (red) and SA (black), (*a*) KH ($m = 0$) and (*b*) k_p^- (0, 2) mode. Here $M_j = 1.16$, $S = 3$ and $St = 0.67$. Jet edges are highlighted in blue.

profiles are seen to be identical. Conversely, in figure 8(*b*) the eigenfunction structures of the k_p^- (0, 2) modes exhibit significant differences between the SS and SA symmetries. Between the two jets the SS solution has higher amplitude than the SA, whilst the opposite occurs away from each jet where the SA solution has a higher amplitude than the SS. The general behaviour of both the KH and k_p^- modes outside the inter-jet region, as would be expected, follows the single-jet case (Tam & Hu 1989). The KH mode peaks along the jet boundary and decays away radially, whilst the k_p^- mode peaks at the centreline before decaying away more slowly. Differences between single- and twin-jet eigenfunctions arise from the aforementioned behaviour in the inter-jet region.

Eigenfunctions for the KH and k_p^- (0, 2) modes can also be found using the finite-thickness model, which allows for insight into how the velocity profile affects the pressure eigenfunctions. These are plotted in figures 9 and 10 for the same jet parameters as in figure 8 with values of δ as 0.12, 0.2 and 0.4. There are two main behaviours that can be seen in figure 9. Within the jet itself, all the models agree well with each other and there is essentially no difference between them. This changes outside the jet core. For SS, figure 9(*a*), increasing shear-layer thickness causes a more rapid radial decay in both the inter-jet and outer regions. This trend is also observed for SA, figure 9(*b*). When considering the region between the jets, the SA eigenfunctions all converge to zero at the midpoint to satisfy the symmetry condition, with the change in δ seen to have only a small effect on the curvature here. There is less agreement observed between the vortex-sheet and finite-thickness model for the KH mode, as shown in figure 10. As was seen for the k_p^- (0, 2) mode, the KH modes predicted using the finite-thickness model decrease in magnitude outside the jet more quickly than in the vortex-sheet model. Inside the jet, the KH modes all follow the same shape but lie apart from each other, with very little overlap of profiles. There is a dissymmetry seen in the amplitude peaks of the KH eigenfunction when considering the finite-thickness model, that is not seen for the vortex-sheet model. As the shear-layer thickness increases, the amplitude of the eigenfunction at the outer mixing layer is seen to decrease slightly.

4.2.2. *Branch and saddle point bounds*

As was shown in § 4.2.1, and noted in Du (1993), the existence region of the k_p^- mode is dependent on jet spacing in twin jets. Here this dependence is considered more closely across multiple S and M_j for the k_p^- (0, 2) mode. This existence region is important when considering the k_p^- mode to close the screech feedback loop, as it then serves as a bound for where screech modes may occur. Any variation in the frequency range over which the

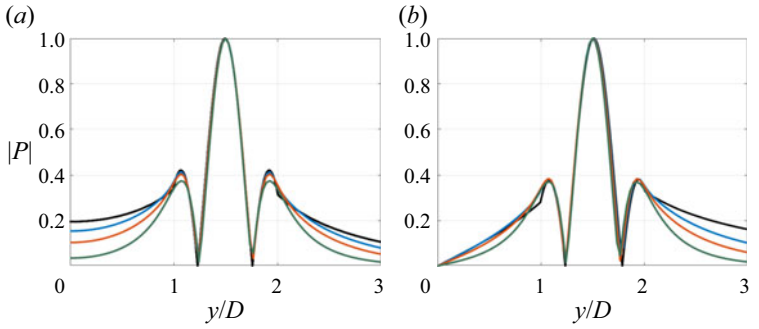

Figure 9. Absolute value of normalised k_p^- $(0, 2)$ pressure eigenfunctions along the y axis for both the vortex-sheet model and varying velocity profiles in the finite-thickness model. Here $M_j = 1.16$, $S = 3$ and $St = 0.67$. Only one jet is shown for both the inter-jet $(y/D < 1)$, inner $(1 < y/D < 2)$ and outer $(y/D > 2)$ regions. Results are shown for (a) SS and (b) SA. Vortex sheet (black), $\delta = 0.12$ (blue), $\delta = 0.2$ (red) and $\delta = 0.4$ (green).

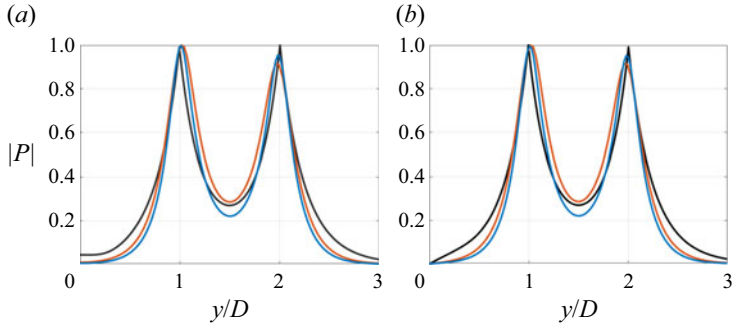

Figure 10. Absolute value of normalised KH $(m = 0)$ pressure eigenfunctions along the y axis for both the vortex-sheet model and varying velocity profiles in the finite-thickness model. Here $M_j = 1.16$, $S = 3$ and $St = 0.67$. Only one jet is shown for both the inter-jet $(y/D < 1)$, inner $(1 < y/D < 2)$ and outer $(y/D > 2)$ regions. Results are shown for (a) SS and (b) SA. Vortex sheet (black), $\delta = 0.12$ (blue) and $\delta = 0.2$ (red). For $\delta = 0.4$, the KH mode has stabilised.

k_p^- modes are propogative can be associated with variations in the frequency range over which screech tones are to be expected. In figure 11 the effect of M_j, S and symmetry on the branch and saddle points are shown for $S = 2, 3, 4, 6$ using the vortex-sheet model. Only M_j up to 1.16 are considered due to the focus of this paper on axisymmetric screech modes. As M_j increases, both the branch and saddle points decrease smoothly, following the same trend as the single-jet case (Mancinelli *et al.* 2019). For the SS symmetry, it is seen in figure 11(a) that changing S influences neither the branch-point nor the saddle-point values. In contrast, the SA symmetry (figure 11b) is observed to be heavily dependent on S. As the jet spacing increases, the SA branch-point frequency decreases, resulting in an increase in the existence region of the k_p^- $(0, 2)$ mode. The saddle points of the SA modes remain unchanged with S.

Variation of branch and saddle points with shear-layer thickness is considered in figure 12, this is achieved through varying the parameter δ of (3.16) in the range 0.12, 0.2 and 0.4. These values were calculated using a ΔSt of 0.01, which may lead to some uncertainty in the values obtained, causing the slight oscillations observed in figure 12. Both the SS, figure 12(a), and the SA symmetry, figure 12(b), have an existence region

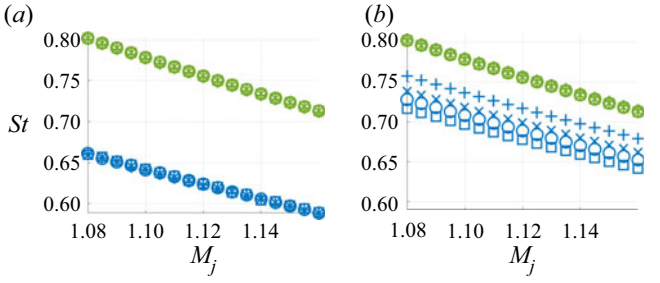

Figure 11. Variation in branch (blue) and saddle (green) points with M_j and S for the k_p^- $(0, 2)$ mode using the vortex-sheet model. Computed for SS (a) and SA (b) with $+$ $S = 2$, $\times$ $S = 3$, $\circ$ $S = 4$ and $\square$ $S = 6$.

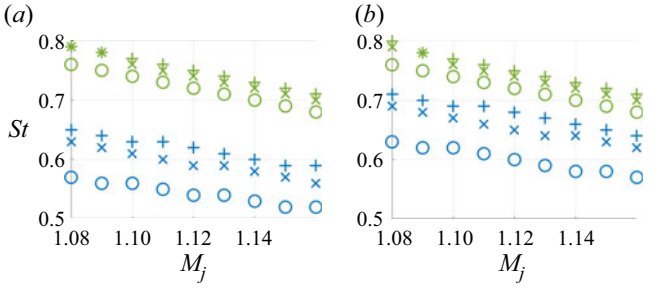

Figure 12. Variation in branch (blue) and saddle (green) points with M_j and δ for the k_p^- $(0, 2)$ mode using the finite-thickness model. Computed for (a) SS and (b) SA. Here $S = 3$ with $+$ $\delta = 0.12$, $\times$ $\delta = 0.2$ and $\circ$ $\delta = 0.4$.

that varies with δ. This is in line with the single-jet case, which also exhibited this behaviour (Mancinelli *et al.* 2021). Across all values of δ the existence region of SS is greater than SA. In figure 12 the saddle points also have a dependence on δ and decrease slightly as it increases. When using the finite-thickness model, figure 12, the existence region of SA symmetry is noticeably greater than that found with the vortex-sheet model, figure 11. Thus, when considering a screech feedback loop closed by the k_p^- $(0, 2)$ mode, the finite-thickness model predicts a larger range over which SA symmetry screech tones may be supported.

4.3. *Predictions of screech frequency*

4.3.1. *Single jet*

Screech-frequency predictions are first preformed for the single-jet system. Such an analysis has been done previously using both a vortex-sheet and finite-thickness model (Mancinelli *et al.* 2021). The equivalent predictions are performed using the experimental set-up considered here for both models. Formulation for the single-jet vortex-sheet model is given by (3.11), whilst the finite-thickness formulation follows § 3.2 without the domain extension, and does not require a discretisation in θ. Predictions are performed using (3.17) over a parameter range of $s = 2 - 6$, $p = 2 - 6$ and $\phi = 0, \frac{1}{4}, \frac{1}{2}, 1$. Acoustics for the single jet are presented in figure 13 with predictions from the vortex-sheet model overlaid along with the branch and saddle points of the k_p^- $(0, 2)$ mode. Best agreement was observed for parameters $s = 4$, $\phi = 0$ and $p = 3$ for the A1 mode, and $s = 4$, $\phi = 0$ and $p = 4$ for the A2 mode. These values are summarised in table 3. Agreement between the model

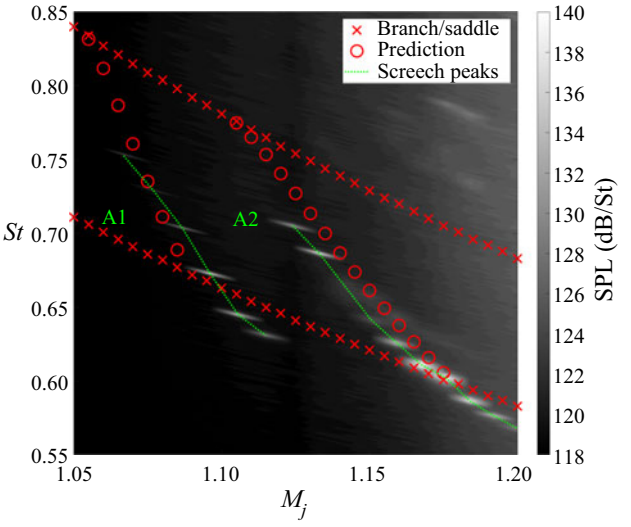

Figure 13. Sound pressure levels (dB/St) measured for the single-jet system running at several M_j. Screech-frequency predictions using the vortex-sheet model are shown, along with k_p^- (0, 2) branch and saddle points. Lines highlighting the screech peaks are included. Parameters used for these predictions are $s = 4$, $p = 3$ (A1 mode), 4 (A2 mode) and $\phi = 0$.

Mode	s	p	ϕ
A1	4	3	0
A2	4	4	0

Table 3. Parameters used for single-jet vortex-sheet model predictions.

and experimental data is good; however, for each of the A1 and A2 screech modes, there is an over-prediction of the frequency at lower M_j and an under-prediction at higher M_j. The branch points of the k_p^- (0, 2) modes sit just above the end of each tone and so do not coincide precisely with the cutoff of the screech tones. Compared with the previous work of Mancinelli *et al.* (2021), the key difference is the value of the phase difference between reflection coefficients, ϕ, used for the screech-frequency predictions. They had found best agreement using $\phi = 1/4$ whereas here that agreement is found for $\phi = 0$, the reflection coefficients being in-phase. This discrepancy would be due to differences in the two facilities, as the screech feedback loop has been noted to display facility sensitivity (Edgington-Mitchell 2019). In this case, an example being the lip thickness of the nozzle that is 15 % in the current work and 3 % previously (Mancinelli *et al.* 2021).

The equivalent predictions of screech frequency for a single jet using the finite-thickness model are overlaid on the experimental data in figure 14, also shown are the branch and saddle points of the k_p^- (0, 2) mode. The hyperbolic tangent profile of (3.16) is used with a value of $\delta = 0.2$ for the velocity profile. This value is chosen to match the value that will be used for twin-jet calculations, and a justification is provided in Appendices B and C. As before, the parameter range of $s = 2 - 6$, $p = 2 - 6$ and $\phi = 0, \frac{1}{4}, \frac{1}{2}, 1$ is considered. Best agreement is observed for $s = 4$, $\phi = 0$ and $p = 4$ for the A1 mode, and $s = 4$, $\phi = 0$ and $p = 5$ for the A2 mode, and these parameters are summarised in table 4. Compared with

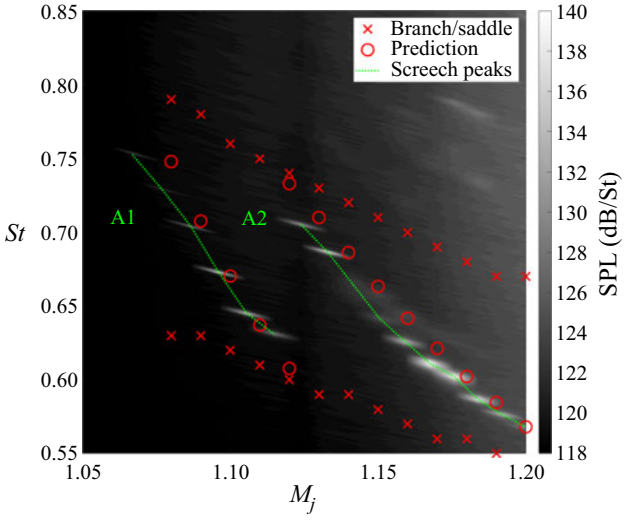

Figure 14. Sound pressure levels (dB/St) measured for the single-jet system running at several M_j. Screech-frequency predictions using the finite-thickness model with $\delta = 0.2$ are shown, along with with k_p^- $(0, 2)$ branch and saddle points. Lines highlighting the screech peaks are included. Parameters used for these predictions are $s = 4$, $p = 4$ (A1 mode), 5 (A2 mode) and $\phi = 0$.

Mode	s	p	ϕ
A1	4	4	0
A2	4	5	0

Table 4. Parameters used for single-jet finite-thickness model predictions.

the previous results from the vortex sheet, figure 13, the predictions here align more closely with the experimental screech tones and match them in slope. Thus utilising a model with a more realistic velocity profile is seen to result in better agreement with the experimental data. This agrees with the previous study of Mancinelli *et al.* (2021) who observed best agreement between model and data for identical velocity profile and parameters as given in table 4. Comparing tables 3 and 4 highlights that the values of p/s are $\neq 1$ (A1) and $= 1$ (A2) for the vortex-sheet model, whilst $= 1$ (A1) and $\neq 1$ (A2) for the finite-thickness model. This further indicates an improvement when moving to the finite-thickness model as these p/s ratios align with results from Nogueira *et al.* (2022*a*).

4.3.2. *Twin jet*

Predictions made using a vortex-sheet model can achieve strong qualitative agreement with experiments, as seen previously for the single jet in § 4.3.1. Given the success of such a simple model in the prediction of single-jet screech, its performance is now considered for the twin-jet problem. In figure 15 predictions using the twin-jet vortex-sheet model are plotted over experimental acoustic data using (3.10) and (3.17). A parameter range of $s = 2 - 6$, $p = 2 - 6$ and $\phi = 0$, $\frac{1}{4}$, $\frac{1}{2}$, 1 was considered with best agreement found between the model and experimental data for $s = 5$, $\phi = 0$ and $p = 4$ for A1 equivalent screech modes and $s = 5$, $\phi = 0$ and $p = 5$ for A2 equivalent screech modes.

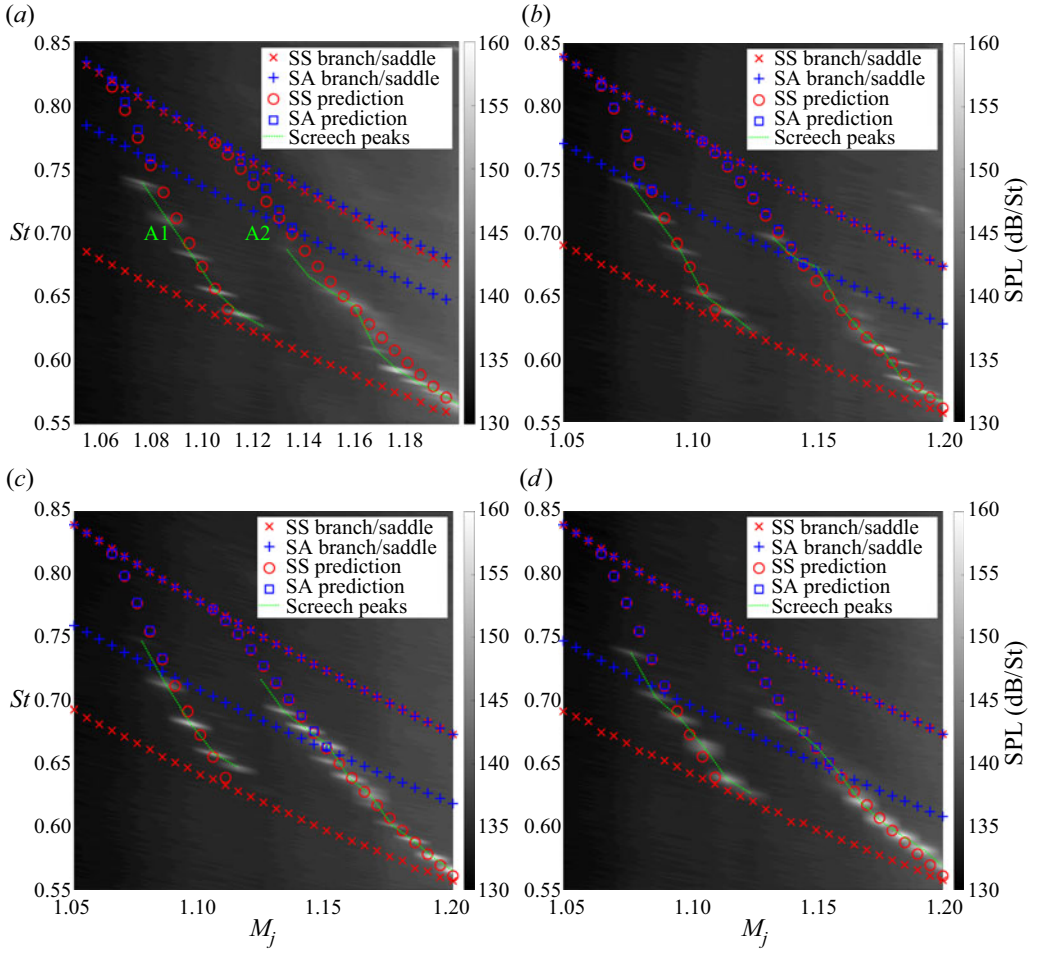

Figure 15. Sound pressure levels (dB/St) measured for the twin-jet system running at several M_j and spacings (*a*) $S = 2$, (*b*) 3, (*c*) 4 and (*d*) 6. Screech-frequency predictions using the vortex-sheet model are shown for both SS (○, red) and SA (□, blue) symmetries. Along with k_p^- (0, 2) branch and saddle points for SS (×, red) and SA (+, blue). Lines highlighting the screech peaks are included. Parameters used for these predictions are $s = 5, p = 4$ (A1 mode), 5 (A2 mode) and $\phi = 0$.

These parameters are summarised in table 5. The branch and saddle points for the k_p^- (0, 2) mode are also shown in figure 15. The predictions for SS symmetry are qualitatively close to the experimental peaks. However, in a more quantitative evaluation, the model suffers from under-prediction at higher M_j and over-prediction at lower M_j for both the A1 and A2 branches. This results in the difference in screech tone variation with M_j between predictions and data in figure 15. These results are comparable to those of the single jet, figure 13 and Mancinelli *et al.* (2021), which displayed the same level of agreement between model and experiment. A key difference between the single- and twin-jet predictions are the parameters used, given in tables 3 and 5. When moving from the single jet to the twin jet, best agreement is found at greater values of s and p, suggesting that the downstream reflection point of resonance increases for a twin jet. There is a sharp bounding of both the A1 and A2 axisymmetric screech modes by the SS k_p^- (0, 2) branch points in figure 15, and these screech modes lie entirely within the propagative range of

Mode	s	p	ϕ
A1	5	4	0
A2	5	5	0

Table 5. Parameters used for twin-jet vortex-sheet model predictions.

the SS k_p^- (0, 2). This is in contrast to the single-jet vortex-sheet model where the branch points were unable to bound the screech tones, highlighting the improvements found when moving to a twin-jet model. When considering the SA k_p^- (0, 2) propagative region, the screech modes are observed to lie predominantly outside of it. At $S = 2$, figure 15(a), there is no overlap, whereas a slight overlap is seen for $S = 3$, figure 15(b), which increases with increasing S in figures 15(c) and 15(d). Thus, the vortex-sheet model suggests that the axisymmetric screech modes observed in a twin-jet system are predominantly SS symmetry for low spacings, and that there are only small regions where SA symmetry could be supported. In the regions where both SS and SA symmetry are permitted the model produces identical predictions for both symmetries, providing no clear way to determine which symmetry the screech mode is expected to be.

Predictions of the screech frequency for the finite-thickness model are obtained using (3.17) with the k_p^- (0, 2) and KH wavenumbers computed from (3.15). The value of δ used in (3.16) is 0.2, which is justified through fitting velocity profiles to experimental particle image velocimetry (PIV) data and considering the region in which the KH mode is unstable (see Appendix B). The same parameter range of $s = 2 - 6$, $p = 2 - 6$ and $\phi = 0, \frac{1}{4}, \frac{1}{2}, 1$ was considered; with best agreement found for $s = 4$, $\phi = 0$ and $p = 4$ for the A1 equivalent screech modes, and $s = 4$, $\phi = 0$ and $p = 5$ for the A2 equivalent screech modes, summarised in table 6. These screech-frequency predictions, along with the branch and saddle points of the k_p^- (0, 2) mode, are plotted over the experimental data in figure 16. The parameters used here for best agreement match those found for the single-jet finite-thickness model, table 4. This results in the same p/s ratios ($= 1$ or $\neq 1$) as were seen for the single jet, suggesting that the shock-cell wavenumber (dominant or sub-optimal) associated with each of the A1 or A2 screech modes is the same for the twin-jet system as it is for the single jet. Considering first the branch and saddle points of the k_p^- (0, 2) mode, the screech modes lie entirely within the SS propagative region but there is a less-sharp bounding by the branch and saddle points for this value of δ. The SA propagative region is larger for the finite-thickness model than the vortex-sheet model for all S and, by $S = 6$ (figure 16d), the screech tones are completely bounded by it. Although there is not a sharp lower bound on the screech tones by the SS branch points, as was observed using the vortex-sheet model in figure 15, the saddle points lie significantly closer to the screech tones. Overall this serves as a closer bounding of the screech tones by the SS branch and saddle points, highlighting an immediate improvement in moving from the vortex-sheet model to the finite-thickness model for twin jets. In addition, changing the parameter δ (or equivalently, choosing a position further upstream/downstream for the analysis) may lead to branch points closer to the lower bounds of the screech tones observed experimentally (Mancinelli *et al.* 2021; Nogueira & Edgington-Mitchell 2021). Predictions obtained with the finite-thickness model offer a clear improvement over those found with the vortex-sheet model, with the slope of the prediction curve aligning closely with the screech tones themselves. This improvement when moving from a vortex-sheet to finite-thickness model matches what was observed for the single jet in § 4.3.1. In regions

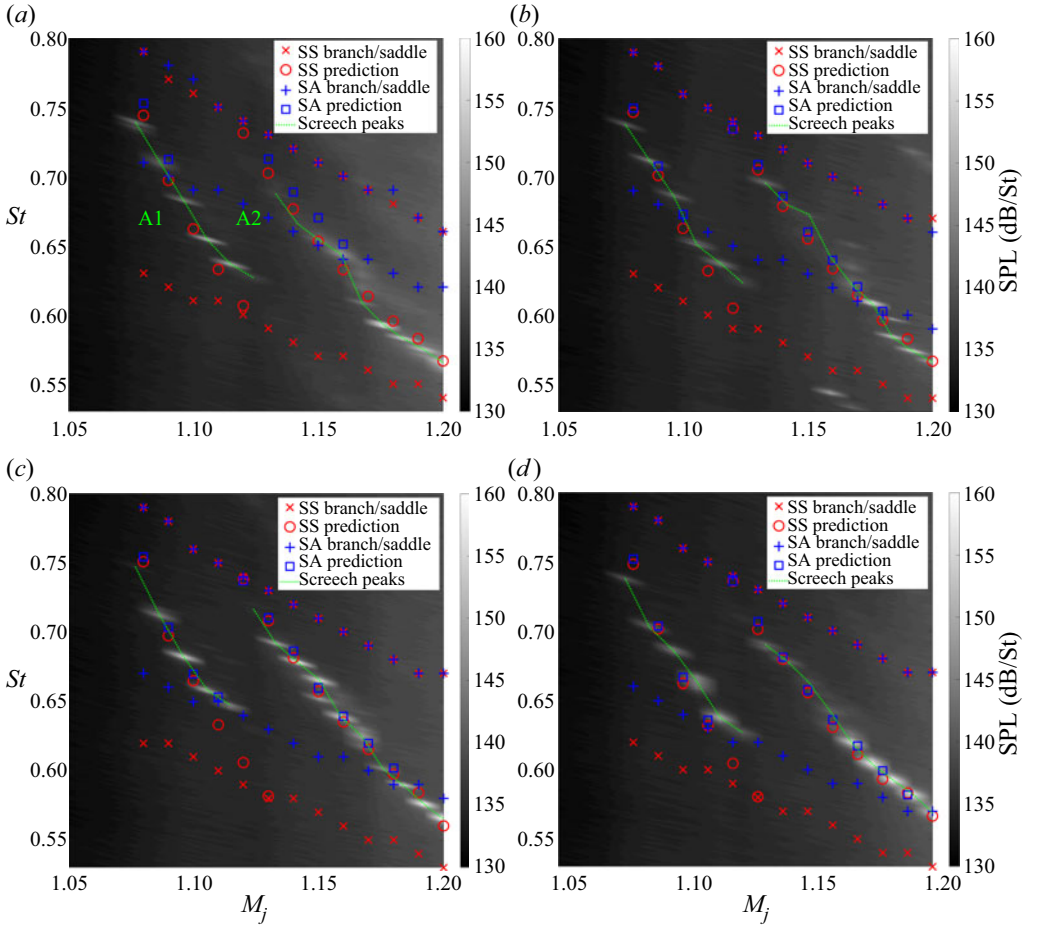

Figure 16. Sound pressure levels (dB/St) measured for the twin-jet system running at several M_j and spacings (*a*) $S = 2$, (*b*) 3, (*c*) 4 and (*d*) 6. Screech-frequency predictions using the finite-thickness model are shown for both SS (○, red) and SA (□, blue) symmetries. Along with k_p^- (0, 2) branch and saddle points for SS (×, red) and SA (+, blue). Lines highlighting the screech peaks are included. Parameters used for these predictions are $s = 4$, $p = 4$ (A1 mode), 5 (A2 mode) and $\phi = 0$.

Mode	s	p	ϕ
A1	4	4	0
A2	4	5	0

Table 6. Parameters used for twin-jet finite-thickness model predictions.

where the twin-jet finite-thickness model predicts both SS and SA symmetry there are only slight differences seen between the predictions. While this differs from the vortex-sheet model that saw identical predictions, it is still not enough to give any indication of a preferential screech symmetry.

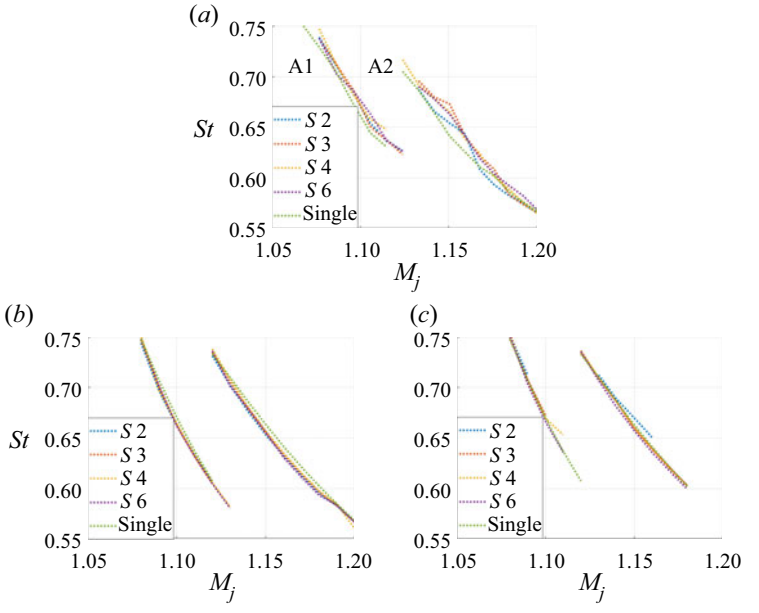

Figure 17. Screech-frequency peaks of the A1 and A2 axisymmetric screech modes from experiment and predicted by the finite-thickness model. These predictions use the same parameters as tables 4 and 6 for $S = 2$, 3, 4, 6 and the single jet. (*a*) Experimental data, (*b*) SS and (*c*) SA.

4.3.3. *Discussion*

In figure 17(*a*) the screech frequencies of the A1 and A2 axisymmetric screech modes, obtained experimentally, are compared across multiple jet separations and with the single jet. It can be seen that there is near negligible change in screech frequency for the A1 mode, whilst the A2 mode exhibits some slight differences but is also mostly unchanged with spacing. This suggests, primarily for the A1 mode, that the screech frequency is not affected by the jet separation. Figures 17(*b*) and 17(*c*) compare the finite-thickness model screech-frequency predictions for both SS and SA symmetry. For SS symmetry, it is seen that the prediction lines lie together with no difference for S, aside from the single-jet prediction that sits just above the others. The SA symmetry, however, exhibits small differences in the prediction lines with spacing and these differences display a noticeable trend with the screech-frequency prediction decreasing with increasing S. From this it could be suggested that the A1 screech mode is of SS symmetry, as both the experiment and model predictions are unchanged with S. These results do not provide any suggestion for the symmetry of the A2 mode.

The branch points of the k_p^- $(0, 2)$ SA modes are seen to be sensitive to two main geometric characteristics of the system: S and the shear-layer thickness. From figure 12 these branch points, for the twin-jet finite-thickness model, decrease in frequency as the shear-layer thickness of the mean flow is increased. This then influences where the model predicts SA symmetry modes to occur, as by considering axial locations further downstream when constructing the mean flow it increases the range of frequencies over which the SA k_p^- mode exists. As such, it could be possible to observe a screech tone of SA symmetry outside of the region predicted by the finite-thickness model in figure 16. This would then indicate that the k_p^- mode is generated at a distance further downstream than was considered by the mean flow utilised here. The dependence on S by the SA

branch points was observed using both twin-jet vortex-sheet and finite-thickness models in figures 11 and 12. It is not currently clear why the SA modes in particular are affected so strongly. The trend, decreasing branch point frequency with increasing S, suggests that for lower jet separations, where the jets may be assumed more strongly coupled, this coupling interferes with the propagation of the SA k_p^- $(0, 2)$ mode in some way. Further work to determine the precise nature of this interaction is required and should shed light more generally on the behaviour of the k_p^- mode.

When considering the vortex-sheet model screech-frequency predictions for both a single jet, § 4.3.1, and twin jet, § 4.3.2, it becomes clear that a single-jet model could not be applied in an attempt to understand twin-jet screech tones. A primary difference for this is the performance of the two models. The twin-jet model is able to bound the screech modes with the branch points of the SS k_p^- $(0, 2)$ mode (figure 15), whereas such agreement cannot be seen for the single jet where the branch points lie just above the lowest frequencies of the screech modes (figure 13). Additionally, a single-jet model, by construction, cannot provide any information about symmetry. This would leave an important aspect of the twin-jet system unable to be considered. By moving to the twin-jet vortex-sheet model it provides an indication of where each symmetry, SS or SA, could be expected to occur for the screech modes.

Vortex-sheet models utilise an idealised 'top-hat' velocity profile that is most accurate very close to the nozzle. For considerations of phenomena that occur at axial locations further downstream, using a finite-thickness model allows for a more realistic velocity profile to be used. Increasing the complexity of the model, by moving to a twin-jet finite-thickness model, results in better agreement with data (figure 16) and allows for the effect of the mean flow to be considered. The region in which SA symmetry screech modes could be expected to occur also increases when moving to the twin-jet finite-thickness model.

The present results indicated the potential for both SS and SA symmetries to be observed experimentally for the A1 and A2 screech modes. In regions where both symmetries are supported, either by the vortex-sheet or finite-thickness twin-jet model, neither model provides enough information to clearly determine a preferred symmetry. The twin-jet finite-thickness model does propose slight differences between SS and SA screech frequencies, with the SA symmetry always occurring at the higher frequency (figure 16), whereas screech frequencies from the twin-jet vortex-sheet model are near identical for the two symmetries (figure 15). The difficulty in discerning symmetry may be due to a competition between screech tones of opposing symmetry. The dominant resonance loop will then be determined by the gain of the resonance loop associated with either SS or SA symmetry. Such a competition between modes was previously put forth by Bell *et al.* (2021) as a possible explanation for the intermittent coupling they observed for round twin jets at higher Mj. For the lower M_j considered here, similar intermittency between symmetry may also be occurring, with the current models only able to indicate the competing symmetries. An alternative method could be required, such as the complex-valued model of Mancinelli *et al.* (2021) or the spatially periodic analysis of Nogueira *et al.* (2022*b*), to determine the dominant symmetry in such regions where both SS and SA are supported.

Finally, both twin-jet models, vortex sheet and finite thickness, assume that the twin-jet system is coupled. Due to this the models cannot provide any insight into potential uncoupling of the jets, a behaviour that has been observed to occur at higher M_j (Bell *et al.* 2021).

5. Conclusions

This investigation used both a vortex-sheet and finite-thickness model to analyse resonance in an under-expanded supersonic twin-jet system running at low supersonic Mach numbers, where the flow is expected to be dominated by axisymmetric disturbances in each jet. Characteristics of both the KH and k_p^- $(0, 2)$ modes were studied using the models, allowing identification of the frequency range over which resonance may occur. The range over which the k_p^- $(0, 2)$ mode is propagative differs depending on the jet symmetry, SS or SA, the jet spacing, S, and the velocity profile used when considering the finite-thickness model. These propagative regions in the vortex-sheet model, for SS and SA, bound the experimental screech tones well, in particular the SS branch points that provide a sharp lower bound for the A1 and A2 modes. For each S, the vortex-sheet model generally over-predicts the screech frequency for low M_j and under-predicts them for high M_j, but still provides qualitative agreement to the data. Better agreement was seen for the finite-thickness model with predictions closely aligning with the experimental data, resulting in stronger agreement than the vortex-sheet model. Neither model was able to distinguish between predictions of SS and SA symmetry for the screech tones, with only slight differences observed for the finite-thickness model, indicating a potential limitation. It is worth recalling that the screech-frequency predictions made in § 4.3 use linear locally parallel models, and the agreement observed between them and the experimental data is very favourable. The improvement seen in moving from a vortex-sheet to finite-thickness model, along with the prediction parameters used for best agreement, follows what was seen for the single-jet case. This similarity with the single-jet case, along with the strong agreement between the twin-jet models and data, suggests that the feedback loop operating in single and twin jets share similarities and the resonance feedback loop for axisymmetric screech tones in round twin-jets is closed through the twin-jet k_p^- $(0, 2)$ mode.

Funding. This work was supported by the Australian Research Council under the Discovery Project Scheme: DP190102220. M.N.S. is supported through an Australian Government Research Training Program Scholarship. Computational facilities supporting this project include the Multi-modal Australian ScienceS Imaging and Visualisation Environment (MASSIVE).

Declaration of interests. The authors report no conflict of interest.

Author ORCIDs.
Michael N. Stavropoulos https://orcid.org/0000-0003-3802-238X;
Matteo Mancinelli https://orcid.org/0000-0002-7332-4335;
Peter Jordan https://orcid.org/0000-0001-8576-5587;
Vincent Jaunet https://orcid.org/0000-0002-6272-1431;
Joel Weightman https://orcid.org/0000-0002-6886-3393;
Daniel M. Edgington-Mitchell https://orcid.org/0000-0001-9032-492X;
Petrônio A.S. Nogueira https://orcid.org/0000-0001-7831-8121.

Appendix A. Matrix operators for finite-thickness formulation

The spatial eigenvalue problem described by (3.15) is a simplified representation of a third-order eigenvalue polynomial problem and as such can be expressed as (Lajús *et al.* 2019; Nogueira & Edgington-Mitchell 2021)

$$\begin{bmatrix} \mathbf{0} & \boldsymbol{I} & \mathbf{0} \\ \mathbf{0} & \mathbf{0} & \boldsymbol{I} \\ -\boldsymbol{A_0} & -\boldsymbol{A_1} & -\boldsymbol{A_2} \end{bmatrix} \begin{bmatrix} \hat{P} \\ k\hat{P} \\ k^2\hat{P} \end{bmatrix} = k \begin{bmatrix} \boldsymbol{I} & \mathbf{0} & \mathbf{0} \\ \mathbf{0} & \boldsymbol{I} & \mathbf{0} \\ \mathbf{0} & \mathbf{0} & -\boldsymbol{A_3} \end{bmatrix} \begin{bmatrix} \hat{P} \\ k\hat{P} \\ k^2\hat{P} \end{bmatrix}, \tag{A1}$$

with each operator $\boldsymbol{A_i}$ being the coefficient of $k^i\hat{P}$, respectively (Bridges & Morris 1984), and defined as

$$\left.\begin{aligned}
\boldsymbol{A_3} &= -U + \frac{\bar{\rho}U^3}{\gamma\bar{P}},\\
\boldsymbol{A_2} &= \omega\left(1 - \frac{3U^2\bar{\rho}}{\gamma\bar{P}}\right),\\
\boldsymbol{A_1} &= U\frac{\partial^2}{\partial r^2} + \frac{U}{r^2}\frac{\partial^2}{\partial\theta^2} + \left(\frac{U}{r} + \frac{U}{\gamma\bar{P}}\frac{\partial\bar{P}}{\partial r} - \frac{U}{\bar{\rho}}\frac{\partial\bar{\rho}}{\partial r} - 2\frac{\partial U}{\partial r}\right)\frac{\partial}{\partial r}\\
&\quad + \left(\frac{2\mathrm{i}\mu U}{r^2} + \frac{U}{\gamma\bar{P}r^2}\frac{\partial\bar{P}}{\partial\theta} - \frac{U}{\bar{\rho}r^2}\frac{\partial\bar{\rho}}{\partial\theta} - \frac{2}{r^2}\frac{\partial U}{\partial\theta}\right)\frac{\partial}{\partial\theta}\\
&\quad + \frac{3U\omega^2\bar{\rho}}{\gamma\bar{P}} - \frac{\mu^2 U}{r^2} + \frac{\mathrm{i}\mu U}{\gamma\bar{P}r^2}\frac{\partial\bar{P}}{\partial\theta} - \frac{\mathrm{i}\mu U}{\bar{\rho}r^2}\frac{\partial\bar{\rho}}{\partial\theta} - \frac{2\mathrm{i}\mu}{r^2}\frac{\partial U}{\partial\theta},\\
\boldsymbol{A_0} &= -\omega\frac{\partial^2}{\partial r^2} - \frac{\omega}{r^2}\frac{\partial^2}{\partial\theta^2} + \left(-\frac{\omega}{r} - \frac{\omega}{\gamma\bar{P}}\frac{\partial\bar{P}}{\partial r} + \frac{\omega}{\bar{\rho}}\frac{\partial\bar{\rho}}{\partial r}\right)\frac{\partial}{\partial r}\\
&\quad + \left(-\frac{2i\mu\omega}{r^2} - \frac{\omega}{\gamma\bar{P}r^2}\frac{\partial\bar{P}}{\partial\theta} + \frac{\omega}{\bar{\rho}r^2}\frac{\partial\bar{\rho}}{\partial\theta}\right)\frac{\partial}{\partial\theta}\\
&\quad + \frac{\omega\mu^2}{r^2} - \frac{\bar{\rho}\omega^3}{\gamma\bar{P}} - \frac{\mathrm{i}\mu\omega}{\gamma\bar{P}r^2}\frac{\partial\bar{P}}{\partial\theta} + \frac{\mathrm{i}\mu\omega}{\bar{\rho}r^2}\frac{\partial\bar{\rho}}{\partial\theta},
\end{aligned}\right\} \tag{A2}$$

with parameters as described in § 3.2.

Appendix B. Choice of velocity profile

When using the finite-thickness model, a hyperbolic tangent velocity profile given by (3.16) is applied to each jet. A required parameter of the profile is δ, which characterises the shear-layer thickness. To determine an appropriate value for this parameter, PIV data from Mancinelli *et al.* (2021) for the single jet at M_j 1.08, 1.12 and 1.16 is considered and (3.16) is fit to the data at different axial locations. The results of this procedure are presented in figure 18 and assist in locating an appropriate value of δ. A further consideration is that the KH mode stabilises as δ increases that suggests an upper bound to the value of δ that can be chosen. This effect is illustrated in figure 19 and it can be seen that the growth rate of the KH mode decreases quickly with δ at higher St number. With the focus of this paper on the axisymmetric screech modes, that occur at high St, the value of δ must be chosen such that the KH mode is still unstable at these St. As such, when considering both figures 18 and 19, $\delta = 0.2$ seems to be an appropriate value that follows both constrains. This value corresponds to the region within the first few axial diameters of the jet, from figure 18, which is where screech modes are expected to be dominant (Edgington-Mitchell *et al.* 2021) and maintains an unstable growth rate of the KH mode at high St, from figure 19. Considerations of the finite-thickness model for a single jet use the same value of δ for consistency. A full parameterisation outlining the regions where the KH mode becomes stable for a twin jet will form part of a future work.

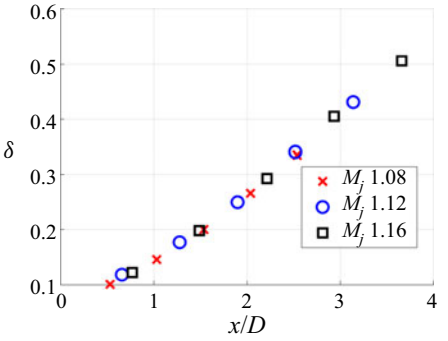

Figure 18. Values of the shear-layer characterisation parameter δ obtained when fitting the hyperbolic tangent profile to single-jet PIV data. Several axial locations (x/D) are considered for M_j 1.08, 1.12 and 1.16.

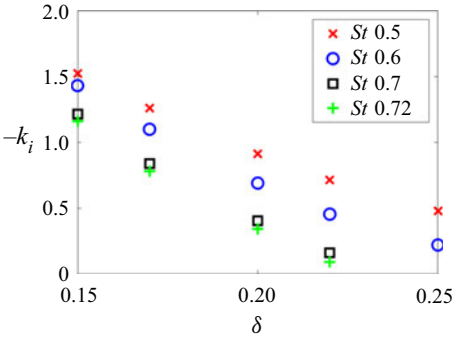

Figure 19. Growth rate of the axisymmetric twin-jet KH instability with shear-layer characterisation parameter δ for SS symmetry, $S = 3$ and $M_j = 1.12$ at $St = 0.5$, 0.6, 0.7 and 0.72.

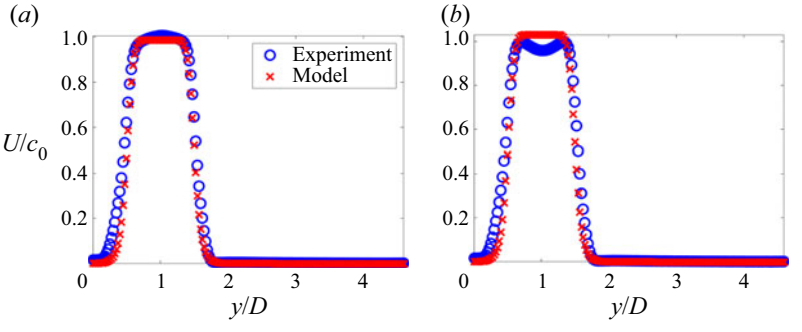

Figure 20. Comparison between the modelled, tanh superposition and experimental, PIV data, velocity profiles for an $S = 2$ twin jet at $x/D = 2$. Results are shown for (*a*) $M_j = 1.1$ and (*b*) $M_j = 1.16$.

Appendix C. Validation of velocity profile

To validate the superimposed tanh velocity profile chosen in Appendix B, it is compared with experimental twin-jet PIV data. The data was collected at the same facility as described in § 2. Seeding of the flow used paraffin oil delivered via an in-house seeder. Images were captured using an ImperX B6640M camera with resolution 6576 × 4400 pixels. A total of 8000 images were taken at both M_j considered, 1.1 and 1.16,

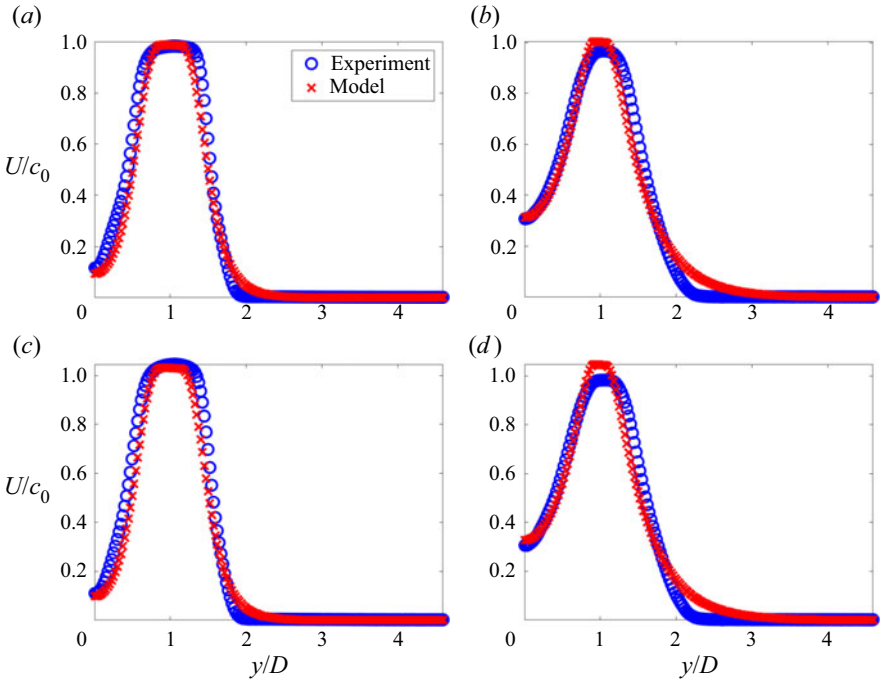

Figure 21. Comparison between the modelled (tanh superposition), and experimental (PIV), velocity profiles for an $S = 2$ twin jet at, (*a*) $M_j = 1.1$ and $x/D = 3$, (*b*) $M_j = 1.1$ and $x/D = 5$, (*c*) $M_j = 1.16$ and $x/D = 3$ and, (*d*) $M_j = 1.16$ and $x/D = 5$. Values of δ used for the tanh superposition are 0.5 and 0.9 respectively for $x/D = 3$ and 5.

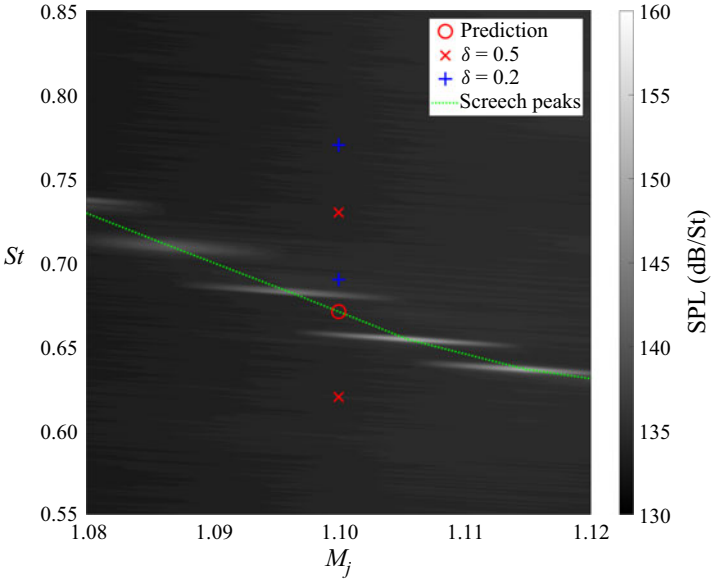

Figure 22. Sound pressure levels (dB/St) measured for the twin-jet system running at several M_j for $S = 2$. A line highlighting the A1 screech peaks is included. The k_p^- (0, 2) branch and saddle points are computed at $M_j = 1.1$ for the SA symmetry using a δ of 0.2 (+, blue), and 0.5 (×, red), respectively. A screech-frequency prediction using the finite-thickness model is shown (○, red), with the KH and k_p^- wavenumbers computed using a δ of 0.2 and 0.5, respectively. Parameters used for this prediction are $s = 4$, $p = 4$ and $\phi = 0$.

for $S = 2$, resulting in 4000 velocity snapshots. Image pairs were processed with the PIVLab toolbox of MATLAB using a multi-grid cross-correlation algorithm (Soria 1996). In figure 20 the velocity profiles of both the PIV and superimposed tanh profile are compared at $S = 2$ for both $M_j = 1.1$ and 1.16, representing the range of jet Mach numbers considered herein. Here the mean velocity field is for an axial position of $x/D = 2$. Strong agreement between the modelled and experimental velocity profiles is observed. This shows that within this work the velocity profile chosen is accurate for modelling waves at $x/D = 2$. Further justification in using a superimposed tanh profile can be found when considering greater axial locations. This is shown in figure 21 for the same jet separation and Mach numbers at axial positions of $x/D = 3$ and 5. A close fit can be obtained here also by adjusting δ to values of 0.5 and 0.9, respectively. Of particular note is the ability of the model to accurately capture the velocity profile in the inter-jet region. From this it is clear that over the low M_j range considered in this work, use of a superimposed tanh profile can accurately model a twin-jet mean flow. Whilst other methods of obtaining a mean flow exist, such as utilising RANS, the availability of the twin-jet PIV data and agreement observed in figures 20 and 21 facilitate the use of a superimposed tanh profile. For completeness, an example screech-frequency prediction is calculated using the superimposed tanh profile of figure 21(*a*) ($\delta = 0.5$) for computing the k_p^- mode wavenumbers, with the wavenumbers of the KH mode obtained as before using $\delta = 0.2$. This is compared with the previous prediction from figure 16(*a*) at $M_j = 1.1$ in figure 22. It indicates how utilising different values of δ, corresponding to different axial positions, can lead to differences in the screech-frequency predictions or even lead to predictions at jet conditions where they did not previously exist (figure 22). This suggests that in future work it may be beneficial to consider the specific axial locations where the k_p^- $(0, 2)$ and KH modes are thought to be generated and compute their respective wavenumbers there for use in prediction models.

References

Bayliss, A. & Turkel, E. 1992 Mappings and accuracy for Chebyshev pseudo-spectral approximations. *J. Comput. Phys.* **101** (2), 349–359.

Bell, G., Cluts, J., Samimy, M., Soria, J. & Edgington-Mitchell, D. 2021 Intermittent modal coupling in screeching underexpanded circular twin jets. *J. Fluid Mech.* **910**, A20.

Bell, G., Soria, J., Honnery, D. & Edgington-Mitchell, D. 2018 An experimental investigation of coupled underexpanded supersonic twin-jets. *Exp. Fluids* **59** (9), 1–19.

Berndt, D.E. 1984 Dynamic pressure fluctuations in the internozzle region of a twin-jet nacelle. *Tech. Rep.* 841540. SAE Technical Paper.

Bridges, T.J. & Morris, P.J. 1984 Differential eigenvalue problems in which the parameter appears nonlinearly. *J. Comput. Phys.* **55** (3), 437–460.

Crow, S.C. & Champagne, F.H. 1971 Orderly structure in jet turbulence. *J. Fluid Mech.* **48** (3), 547–591.

Davies, M.G. & Oldfield, D.E.S. 1962 Tones from a choked axisymmetric jet. I. Cell structure, eddy velocity and source locations. *Acta Acust. United Ac.* **12** (4), 257–267.

Du, Z. 1993 Acoustic and Kelvin–Helmholtz instability waves of twin supersonic jets. PhD thesis, Department of Mathematics, The Florida State University, Florida.

Edgington-Mitchell, D. 2019 Aeroacoustic resonance and self-excitation in screeching and impinging supersonic jets–a review. *Intl J. Aeroacoust.* **18** (2–3), 118–188.

Edgington-Mitchell, D., Jaunet, V., Jordan, P., Towne, A., Soria, J. & Honnery, D. 2018 Upstream-travelling acoustic jet modes as a closure mechanism for screech. *J. Fluid Mech.* **855**, R1.

Edgington-Mitchell, D., Li, X., Liu, N., He, F., Wong, T.Y., Mackenzie, J. & Nogueira, P. 2022 A unifying theory of jet screech. *J. Fluid Mech.* **945**, A8.

Edgington-Mitchell, D., Wang, T., Nogueira, P., Schmidt, O., Jaunet, V., Duke, D., Jordan, P. & Towne, A. 2021 Waves in screeching jets. *J. Fluid Mech.* **913**, A7.

Gojon, R., Bogey, C. & Mihaescu, M. 2018 Oscillation modes in screeching jets. *AIAA J.* **56** (7), 2918–2924.

HARPER-BOURNE, M. & FISHER, M.J. 1974 The noise from shock waves in supersonic jets, noise mechanisms. In *AGARD Conference on Noise Mechanisms* (*AGARD CP-131*), paper 11–1.

JORDAN, P., JAUNET, V., TOWNE, A., CAVALIERI, A.V.G., COLONIUS, T., SCHMIDT, O. & AGARWAL, A. 2018 Jet–flap interaction tones. *J. Fluid Mech.* **853**, 333–358.

KNAST, T., BELL, G., WONG, M., LEB, C.M., SORIA, J., HONNERY, D.R. & EDGINGTON-MITCHELL, D. 2018 Coupling modes of an underexpanded twin axisymmetric jet. *AIAA J.* **56** (9), 3524–3535.

LAJÚS, F.C., SINHA, A., CAVALIERI, A.V.G., DESCHAMPS, C.J. & COLONIUS, T. 2019 Spatial stability analysis of subsonic corrugated jets. *J. Fluid Mech.* **876**, 766–791.

LANDAU, L.D. & LIFSHITZ, E.M. 2013 *Course of Theoretical Physics*. Elsevier.

LEE, W.M. & CHEN, J.T. 2011 Free vibration analysis of a circular plate with multiple circular holes by using indirect BIEM and addition theorem. *Trans. ASME J. Appl. Mech.* **78** (1), 011015.

LESSEN, M., FOX, J.A. & ZIEN, H.M. 1965 The instability of inviscid jets and wakes in compressible fluid. *J. Fluid Mech.* **21** (1), 129–143.

MANCINELLI, M., JAUNET, V., JORDAN, P. & TOWNE, A. 2019 Screech-tone prediction using upstream-travelling jet modes. *Exp. Fluids* **60** (1), 22.

MANCINELLI, M., JAUNET, V., JORDAN, P. & TOWNE, A. 2021 A complex-valued resonance model for axisymmetric screech tones in supersonic jets. *J. Fluid Mech.* **928**, A32.

MANCINELLI, M., MARTINI, E., JAUNET, V., JORDAN, P., TOWNE, A. & GERVAIS, Y. 2023 Reflection and transmission of a Kelvin–Helmholtz wave incident on a shock in a jet. *J. Fluid Mech.* **954**, A9.

MERLE, M.M. 1957 Nouvelles recherches sur les fréquences ultrasonores émises par les jets d'air. In *Annales des Télécommunications*, vol. 12, pp. 424–426. Springer.

MICHALKE, A. 1970 A note on the spatial jet-instability of the compressible cylindrical vortex sheet. *Tech. Rep.* FB-70-51. Deutsche Forschungs-und Versuchsanstalt für Luft-und Raumfahrt.

MICHALKE, A. 1971 Instabilitaet eines kompressiblen runden freistrahis unter beruecksichtigung des einflusses der strahigrenzschichtdicke (Instability of a compressible circular jet considering the influence of the thickness of the jet boundary layer). *Tech. Rep.*, Vol. 19, pp. 319–328. Deutsche Forschungs-und Versuchsanstalt fuer Luft-und Raumfahrt, EV Berlin (West Germany).

MOLLO-CHRISTENSEN, E. 1967 Jet noise and shear flow instability seen from an experimenter's viewpoint. *Trans. ASME J. Appl. Mech.* **34** (1), 1–7.

MORRIS, P.J. 1990 Instability waves in twin supersonic jets. *J. Fluid Mech.* **220**, 293–307.

MORRIS, P.J. 2010 The instability of high speed jets. *Intl J. Aeroacoust.* **9** (1–2), 1–50.

NOGUEIRA, P.A.S. & EDGINGTON-MITCHELL, D.M. 2021 Investigation of supersonic twin-jet coupling using spatial linear stability analysis. *J. Fluid Mech.* **918**, A38.

NOGUEIRA, P.A.S., JAUNET, V., MANCINELLI, M., JORDAN, P. & EDGINGTON-MITCHELL, D. 2022*a* Closure mechanism of the A1 and A2 modes in jet screech. *J. Fluid Mech.* **936**, A10.

NOGUEIRA, P.A.S., JORDAN, P., JAUNET, V., CAVALIERI, A.V.G., TOWNE, A. & Edgington-Mitchell, D. 2022*b* Absolute instability in shock-containing jets. *J. Fluid Mech.* **930**, A10.

PACK, D.C. 1950 A note on Prandtl's formula for the wave-length of a supersonic gas jet. *Q. J. Mech. Appl. Maths* **3** (2), 173–181.

POWELL, A. 1953*a* The noise of choked jets. *J. Acoust. Soc. Am.* **25** (3), 385–389.

POWELL, A. 1953*b* On the mechanism of choked jet noise. *Proc. Phys. Soc.* **66** (12), 1039.

POWELL, A., UMEDA, Y. & ISHII, R. 1992 Observations of the oscillation modes of choked circular jets. *J. Acoust. Soc. Am.* **92** (5), 2823–2836.

RAMAN, G. 1999 Supersonic jet screech: half-century from Powell to the present. *J. Sound Vib.* **225** (3), 543–571.

RAMAN, G., PANICKAR, P. & CHELLIAH, K. 2012 Aeroacoustics of twin supersonic jets: a review. *Intl J. Aeroacoust.* **11** (7–8), 957–984.

RODRÍGUEZ, D. 2021 Wavepacket models for supersonic twin-jets. *AIAA Aviation 2021 Forum*, paper 2121.

RODRÍGUEZ, D., JOTKAR, M.R. & GENNARO, E.M. 2018 Wavepacket models for subsonic twin jets using 3D parabolized stability equations. *C. R. Méc* **346** (10), 890–902.

RODRÍGUEZ, D., STAVROPOULOS, M.N., NOGUEIRA, P.A.S., EDGINGTON-MITCHELL, D. & JORDAN, P. 2022 On the preferred flapping motion of round twin jets. *J. Fluid Mech.* (submitted) arXiv:2210.07665.

SEDEL'NIKOV, T.K. 1967*a* The dispersion relations for multilayer jets and for several jets. In *Physics of Aerodynamic Noise* (ed. A.V. Rimskiy-Korsakov) (Transl. NASA TTF-538, 1969). Nauka Press.

SEDEL'NIKOV, T.K. 1967*b* The frequency spectrum of the noise of a supersonic jet. In *Physics of Aerodynamic Noise* (ed. A.V. Rimskiy-Korsakov) (Trans. NASA Tech. Trans. F-538). Nauka Press.

SEINER, J.M., MANNING, J.C. & PONTON, M.K. 1988 Dynamic pressure loads associated with twin supersonic plume resonance. *AIAA J.* **26** (8), 954–960.

SHAW, L. 1990 Twin-jet screech suppression. *J. Aircraft* **27** (8), 708–715.

SHEN, H. & TAM, C.K.W. 2002 Three-dimensional numerical simulation of the jet screech phenomenon. *AIAA J.* **40** (1), 33–41.

SORIA, J. 1996 An investigation of the near wake of a circular cylinder using a video-based digital cross-correlation particle image velocimetry technique. *Exp. Therm. Fluid Sci.* **12** (2), 221–233.

STAVROPOULOS, M., MANCINELLI, M., JORDAN, P., JAUNET, V., EDGINGTON-MITCHELL, D.M. & NOGUEIRA, P. 2022 Analysis of axisymmetric screech tones in round twin-jets using linear stability theory. In *28th AIAA/CEAS Aeroacoustics 2022 Conference*, paper 3071. American Institute of Aeronautics and Astronautics.

TAM, C.K.W. 1995 Supersonic jet noise. *Annu. Rev. Fluid Mech.* **27** (1), 17–43.

TAM, C.K.W. & HU, F.Q. 1989 On the three families of instability waves of high-speed jets. *J. Fluid Mech.* **201**, 447–483.

TAM, C.K.W. & TANNA, H.K. 1982 Shock associated noise of supersonic jets from convergent-divergent nozzles. *J. Sound Vib.* **81** (3), 337–358.

TOWNE, A., CAVALIERI, A.V.G., JORDAN, P., COLONIUS, T., SCHMIDT, O., JAUNET, V. & BRÈS, G.A. 2017 Acoustic resonance in the potential core of subsonic jets. *J. Fluid Mech.* **825**, 1113–1152.

TREFETHEN, L.N. 2000 *Spectral Methods in MATLAB*. SIAM.

WELCH, P. 1967 The use of fast Fourier transform for the estimation of power spectra: a method based on time averaging over short, modified periodograms. *IEEE Trans. Audio Electroacoust.* **15** (2), 70–73.

WONG, M.H., KIRBY, R., JORDAN, P. & EDGINGTON-MITCHELL, D. 2020 Azimuthal decomposition of the radiated noise from supersonic shock-containing jets. *J. Acoust. Soc. Am.* **148** (4), 2015–2027.

YEUNG, B., SCHMIDT, O.T. & BRÈS, G.A. 2022 Three-dimensional spectral pod of supersonic twin-rectangular jet flow. *AIAA Aviation 2022 Forum*, paper 3345.